JOURNAL OF PROPULSION AND POWER
Vol. 10, No. 4, July–Aug. 1994

Three-Dimensional Analysis of Scramjet Nozzle Flows

Tomiko Ishiguro* and Ryouji Takaki*
National Aerospace Laboratory, Tokyo 182, Japan
and
Tohru Mitani† and Tetsuo Hiraiwa†
Kakuda Research Center, Miyagi 989-15, Japan

Numerical and experimental results of performance in National Aero-Space Plane-like nozzles are compared. The full Navier-Stokes equation with the Baldwin-Lomax turbulence model was adopted to solve the three-dimensional nozzle flows. A code validation study was conducted using pressure and heat-flux distributions measured. The interactions of separation shocks with the main internal flow under overexpanded conditions were investigated. The interaction yields higher performance in scramjet nozzles than that estimated assuming a two-dimensional separation. The losses in the nozzle internal flow and the overexpansion loss were evaluated.

Introduction

HYPERSONIC air-breathing vehicles, such as the National Aero-Space Plane (NASP), will be based on a scramjet system during a major portion of their missions and will require efficient airframe propulsion integration. In this system, the afterbody is designed as a single-expansion ramp-nozzle to minimize friction drag and nozzle weight while extracting thrust from the high-pressure flow on the afterbody. Unlike lower Mach number propulsion systems which develop a large portion of their thrust in the inlet, the scramjet produces thrust only in the divergence sections, especially in the nozzle.

The authors have undertaken a comprehensive experimental and computational investigation of scramjet nozzles.[1,2] To identify the chemical kinetic loss in the nozzle in the studies, a gas generator burning monomethyl-hydrazine and nitrogen tetraoxide was used to produce a hot flow with a total temperature of 3100 K. Cold nitrogen N_2 flow experiments were also conducted to investigate the aerodynamic aspects of the nozzle flows. In these studies, it was possible to estimate nozzle internal performance and the internal losses (the chemical kinetic, the divergence, and the friction losses).

Effects of external flow on the nozzle are also important, because hypersonic vehicles, and especially the single-stage-to-orbit (SSTO), experience large variations in ambient or "back" pressure. The effect of ambient pressure is measured in terms of nozzle pressure ratio (NPR), defined as the ratio between the nozzle total pressure P_0, and the ambient pressure P_a. The off-design operation of the nozzle designed at a given NPR can cause serious performance loss (overexpansion loss).

There have been many experimental and numerical studies on the interactions between the nozzle exhaust plume and the external flow.[3–13] Watanabe[10] observed the flow interaction using a Mach 7.1 wind tunnel. Monta[13] investigated the effects of side-fences on the flowfield using the NASA Langley, 20-in. Mach 6 wind tunnel. Detailed experiments using flow visualization and rake probes were conducted by Spaid and Keener.[6,7] For comparison with experimental findings, Ruffin[11] solved the full Navier-Stokes equation to reproduce the overall features of the nozzle flow interaction with the external flowfield. However, the profiles of the separation vortex differed from that of the experiments because the laminar flow was assumed in the computation. Comprehensive investigation of the flowfield to quantitatively evaluate its effects on nozzle performance has not been completed.

The first subject of this article is the validation of a three-dimensional code using the pressure and heat flux distributions measured using cold N_2 flow. Effects of the interaction on the nozzle performance under off-design conditions are discussed next. Finally, the internal losses and the overexpansion loss are identified with the aid of three-dimensional calculation. The experimental part of this study is presented in Ref. 2.

Numerical Methods and Comparison with Experiments

Numerical Calculation

The nozzle model used in this study (EN_5) is illustrated in Fig. 1. The nozzle was mounted at the exit of a gas generator. The EN_5 nozzle was designed for a gas-generator exit Mach number of 2.9. The flat plate ramp inclined by 15 deg to the axis of the main thrust. The cowl and the two sidefences were aligned with the axis. It is not possible to define the nozzle expansion ratio uniquely for the asymmetric nozzles. The nozzle expansion ratio was defined by the ratio between the projected area of the scramjet nozzle exit in the axis of the main axis and the inlet area of the scramjet nozzle. This definition is the most suitable, physically-meaningful choice, unless the

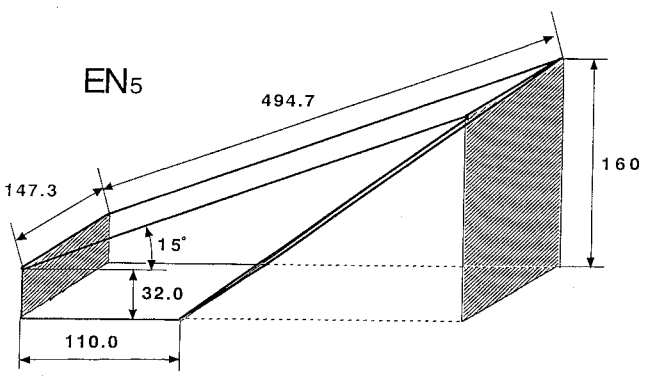

Fig. 1 Scramjet nozzle examined in this study (in mm).

Received Sept. 25, 1993; presented as Paper 93-5059 at the AIAA/DGLR 5th International Aerospace Planes and Hypersonics Technologies Conference, Munich, Germany, Nov. 30–Dec. 5, 1993; revision received Jan. 21, 1994; accepted for publication Jan. 26, 1994.

*Computational Science Division, Jindaiji-Higashi machi, Chofu.
†Ramjet Propulsion Division, National Aerospace Laboratory, Kimigaya 1, Kakuda.

Table 1 Nozzle internal performances (specific impulse in m/s) evaluated by experiments, the JANNAF method, and the three-dimensional viscous code, TVD3D

	Thrust	Friction losses				Internal performances
	$\int P_w\, dA$, m/s	Ramp	Cowl	Side-fences	Total, m/s	I_{sp}, m/s
Experiment[1]	54.0	——	——	——	6.6	47.4
JANNAF method	50.5 (−6.5%)	2.0	3.8	6.6	12.4	38.1 (−20%)
TVD3D	53.0 (−2.0%)	1.62	2.44	3.50	7.56	45.4 (−4.2%)

Table 2 External flow conditions calculated by TVD3D

		NPR	Thrust, m/s		Friction losses, m/s				
Case	Mach	P_0/P_a	$\int P_w\, dA$	$\int P_a\, da$	Ramp	Cowl	Side-fences	Total	I_{sp}, m/s
A	0	968.0	53.0	−6.97	−1.62	−2.44	−3.50	−7.56	38.5
A	0	968.0	52.8	−6.97	−1.61	−3.47	−3.83	−7.91	37.9
B	6	968.0	53.0	−6.97	−1.64	−2.40	−3.51	−7.55	38.4
C	0	96.8	58.2	−69.70	−1.61	−2.48	−3.29	−7.38	−18.9
D	6	96.8	53.8	−69.70	−1.57	−2.46	−3.47	−7.50	−23.4

P_w and P_a are wall and ambient pressure, respectively.

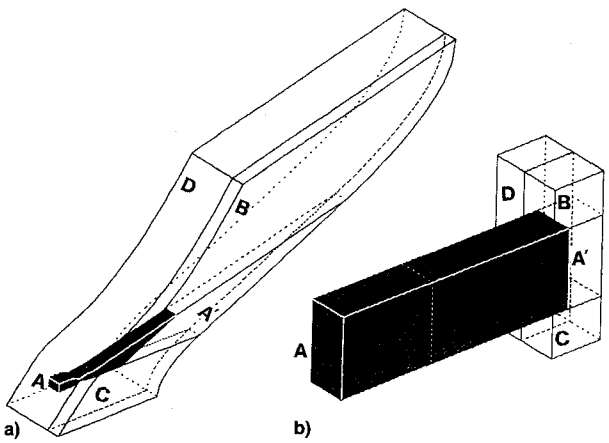

Fig. 2 Mapping to computational space in the TVD3D calculations: a) physical and b) computational space.

wave emerging from the cowl trailing edge interacts with the ramp trailing edge.

Two computational approaches were compared. The first one is the method developed by JANNAF[14] (Table 1). This approach was established by JANNAF for evaluating performance of liquid propellant rockets. The calculation is composed of the one-dimensional equilibrium code (ODE), the one-dimensional kinetic code (ODK), and the two-dimensional kinetic code (TDK). The two-dimensional chemical kinetic (inviscid) code was prepared at the National Aerospace Laboratory and extended for analyzing flows in asymmetric nozzles. The boundary-layer loss or the friction loss (FL) in the nozzles was evaluated by the momentum integral method. The details of this approach and the comparison with experimental results are found in Ref. 1.

For comparison with experimental results, cold N_2 with a total pressure of 0.981 MPa and a total temperature of 293 K was chosen as the working fluid. The internal performance of the scramjet nozzles was estimated using the JANNAF method, and the effect of the external flow was investigated using a three-dimensional code (TVD3D). Effects of windon with Mach 6 and ambient pressure were examined in cases A, A′, B, C, and D in Table 2. The static pressures of the external flow are 0.01 and 0.1 atm, which correspond to NPR = 968 and 96.8, respectively. Nozzle performance was compared assuming an isothermal wall (cases A, B, C, and D) and an adiabatic wall (case A′).

The three-dimensional, implicit time-marching Navier-Stokes solver (TVD3D) is a finite difference code that solves the Reynolds-averaged Navier-Stokes equations in generalized coordinates. The convection term is discretized by the Harten-Yee type, total variation diminishing (TVD) scheme. The scheme was improved to minimize the influence of the grid employed. A diagonal implicit approximate factorization (IAF) scheme was adopted to advance the time step. The ultimate, steady-state solutions were obtained by integrating the time step locally.

The computational grids used in this study were created with an algebraic grid generation code. To map the nozzle internal region and external regions, four grid zones were generated. The surface grid and the boundaries of each zone in the physical and the computational domains are shown in Figs. 2a and 2b. In Fig. 2, zones A and A′ map the nozzle main flow; the other zones are for the external flow region. Zone A denotes the internal flow occupying the gas generator and the scramjet nozzles. The boundary conditions for zone A are the inflow conditions for the left plane. No-slip, adiabatic, or isothermal conditions were applied for the wall condition. The cowl, ramp, and side-fences were assumed to be infinitesimally thin. The front sides of zones A, A′, B, and C were symmetry planes. On the right sides of zones A, B, C and D, the flow variables were extrapolated from the interior (the outflow condition). The planes connected to the external region were subject to the external flow conditions. A two-dimensional numerical result was used to initiate the three-dimensional computation. The initial condition for the two-dimensional calculation was derived from a quasi-one-dimensional result. The pressure and velocity in zones B, C, and D were specified by the ambient values.

The three-dimensional computation on the EN_5 model was performed using nonuniform grids as shown in Fig. 3. The numbers of grids (x direction × y direction × spanwise direction) are given in the figure. The grid in zone A, the most important zone for nozzle performance, was chosen to be 203 in the streamwise direction to resolve the internal flow patterns. A total of 540,000 points were contained in the grid. The minimum y distance between the wall and the adjoining grid was 4×10^{-3} mm. The unit Reynolds number was estimated to be 20×10^6 for the cold N_2 flow. The typical calculation required approximately 14 h of CPU time on a supercomputer (FACOM VP-2600/10).

Measurements of boundary layer, heat transfer, and friction loss indicate the cold N_2 flow to be turbulent.[1] Efficient turbulence models for the Reynolds-averaged Navier-Stokes equations have been sought for practical aerodynamic applications. Of special importance for high-speed compressible flows is the accurate prediction of adverse pressure gradient

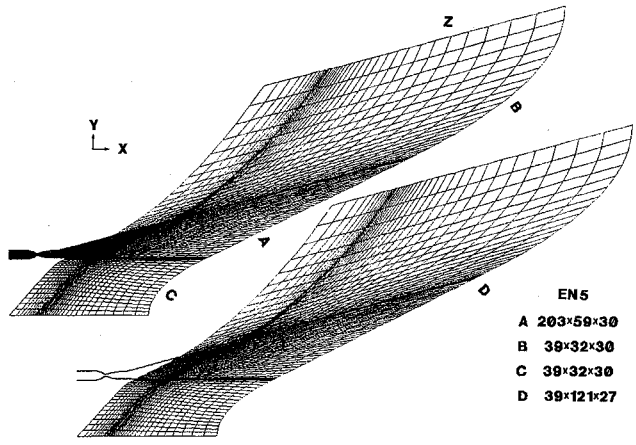

Fig. 3 Grid systems for zones A, B, C, and D in the TVD3D calculations.

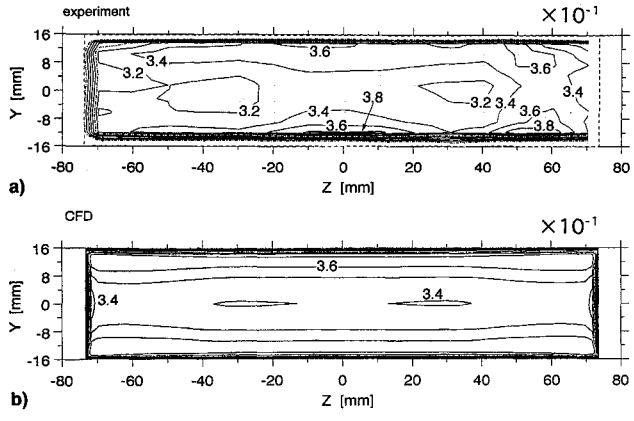

Fig. 4 Comparison of pitot pressure at the entrance of the scramjet nozzle: a) experiment and b) computation.

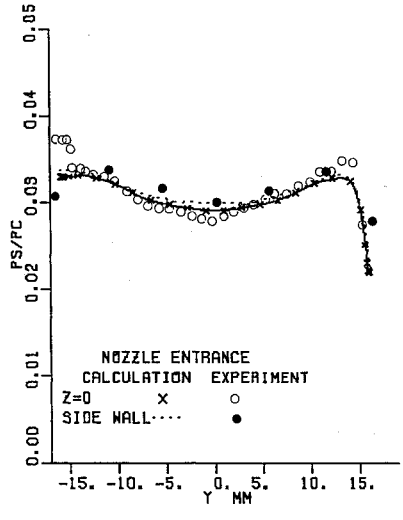

Fig. 5 Comparison of static pressure at the entrance of scramjet nozzle. The computational results are shown by solid and broken lines.

with and without separation. An excellent review can be found in Ref. 15.

As later described in the Discussion, the strong interaction between shock waves and boundary layer was found in our overexpanded nozzle flow.[2] There are a number of studies on the interaction in supersonic inlets.[16-18] Narayanswami et al.[18] carried out a numerical study to simulate the flowfield in the inlet with the Baldwin-Lomax and the k-ε models. They reported that both of the models were able to simulate the overall structure of the interaction between the shock waves and the boundary layer. Therefore, the simplest turbulence

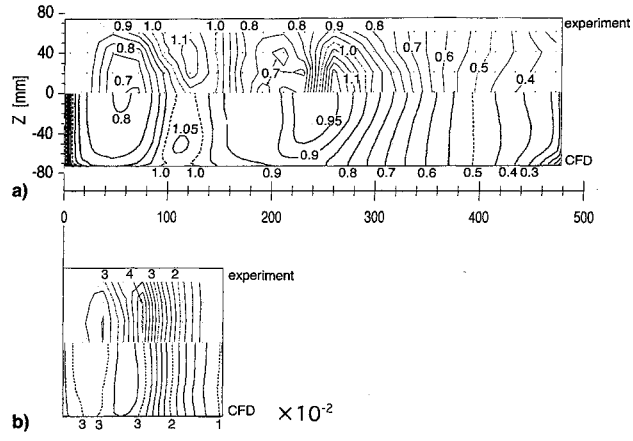

Fig. 6 Comparison of wall pressure in a) the nozzle ramp and b) the cowl. The computational results are shown in the lower portions. X_s, the distance along the scramjet nozzle (mm).

model, the Baldwin-Lomax model, was employed in this numerical study.

Comparison of Pressure Distributions

Before performing the analysis of the scramjet nozzle flow, it is important to investigate the inlet conditions of the nozzle. Figure 4 presents the pitot pressure distribution measured at 182 locations at the inlet of the scramjet nozzle (the exit of gas generator). The pitot pressure was normalized using the total pressure. The experimental result shows that the normalized pitot pressure varies from 0.32 at the center to 0.38 at the lower wall. The pitot pressure distribution obtained by the TVD3D code is shown in Fig. 4b.

The concave profile in the y direction in Fig. 4, and more evident in Fig. 5, was expected for cold N_2 flow because the gas generator was designed to be wave-free for the hot combustion gas. The displacement thickness of the boundary layer developed on the side-fences of the gas generator produced compression waves and yielded the distribution in the spanwise (z) direction in Fig. 4. As a result, the incomplete cancellation of waves generated twin-dips with a lower pressure of $P/P_0 = 0.32$ in the pressure contours in Fig. 4a. The numerical results reproduced the overall variation found in the pitot pressure. However, the variation given by the numerical calculation resulted in a "smoothing out," as compared with the experimental counterpart.

It is more difficult to predict the static pressure than the pitot pressure. In Fig. 5, the numerical results are compared with measured values at $z = 0$ mm using a static probe (○) as well as with the pressure measured at the sidewall (z = 73.7 mm, ●). The higher pressure at $y = -15$ mm is caused by an incident shock wave originating from the leading edge of the probe. The rapid depression found at $y = +14$ mm is the Prandtl-Meyer expansion wave initiated at the point of the ramp deflection. The computational results by TVD3D at the symmetric plane (solid line) and the sidewall (broken line) successfully reproduce the concave nature of the static pressure in the incoming flow to the scramjet nozzle. Thus, these comparisons indicate the adequacy of the TVD3D code for application to the prediction of the scramjet nozzle flow.

Pressure distributions in the cowl and in the ramp are presented in Figs. 6a and 6b. The wall pressure on the ramp and the cowl was measured at 150 stations. The standard deviation in pressure measured was evaluated to be 1.3 kPa in 11 measurements. The wall pressure was normalized by the total pressure ($10^2 P_w/P_0$ in the figures). The standard deviation for P_w/P_0 increased downstream, because the value of P_w decreased. A typical standard deviation for P_w/P_0 was estimated to be 6.3%.

Figure 6b is the isobaric contours derived by TVD3D and Fig. 6a is the experimental counterpart. The twin-dips in the

pitot pressure contours shown in Fig. 4 were reflected as twin-peaks in the nozzle pressure on the cowl (X_s = 70 mm) and the ramp (X_s = 120 mm) in Fig. 6. The depression by the Prandtl-Meyer expansion fan was observed to the cowl ($X_s >$ 70 mm) and the wave reflected from the cowl on the ramp ($X_s >$ 160 mm). A steep pressure rise was found at the cowl (X_s = 70 mm) and the reflection developed into a shock wave on the ramp (X_s = 160 mm). The shock wave was initiated from the gas generator, because the nozzle contour failed to be wave-free for the cold N_2 flow. A thick boundary layer along the side-wall corner was found at the trailing edge of the ramp in the experimental results and the numerical results.

Although the isobaric patterns coincide qualitatively, the compression waves in the experimental results were found to be less sharp in the numerical results. It is also noted that the locations of peaks and dips in the pressure distributions shifted upstream in the computational results. The computation gave a Mach number which is smaller by 5.9% than the experimental result. This implies that the present study is insufficient to evaluate the accurate pitching moment produced in asymmetric nozzles.

These differences from the experimental results are not due to the gridding adopted in these computations. As illustrated in Fig. 3, the grid size in the x direction is sufficiently small, and so several grids are located in the steep P_w variation found at 200 < X_s < 240 on the ramp. The effects of gridding on the wall pressure distribution were also examined using two-dimensional TVD codes to save CPU time. The cases with streamwise grids of 200 (57), 400 (113), and 800 (225) were compared. The number in parentheses denotes the number of grids on the ramp of the scramjet nozzle; they are greater in number than the 22 streamwise measuring stations in the experiment. However, the increased number of grids did not improve the flattened pressure distribution nor the underestimation of Mach number found in Fig. 6 significantly. Therefore, it was concluded that these were caused by the TVD scheme.

The TVD3D code was developed to capture shock waves or strong compression waves in flows. In scramjet nozzle flows, however, an expansion fan initiates from the ramp deflection corner and interacts with the weak compression waves from the gas generator. The Harten-Yee scheme should be improved to capture expansion waves as precisely as it captures compression waves.

Heat-Flux and Skin Friction Coefficient

Pressure distributions can be used to validate inviscid codes. However, viscous codes have to be ultimately checked by means of transport properties of flows. The heat-flux on the scramjet nozzle was measured using thermocouples. The limitations in the spatial resolution and the accuracy of the thermocouples embedded in the nozzle walls were examined by using a heat conduction computer code. The experimental uncertainty in the measurement is illustrated by the error bar in Fig. 7. Because of the small temperature gradient in the cold N_2 flow, the heat-flux observed was low and varied from 15 to 2 kW/m^2 on the ramp. The rapid increase of heat-flux at the trailing edge was caused by the thin boundary layer found in Fig. 6. The variations of heat-flux can be correlated with those of Reynolds number along the wall. The effect of Mach number on the heat-flux was found to be weak. The solid lines in Fig. 7 are the calculated results by TVD3D. The computational values on the ramp and the cowl agreed with the experimental results.

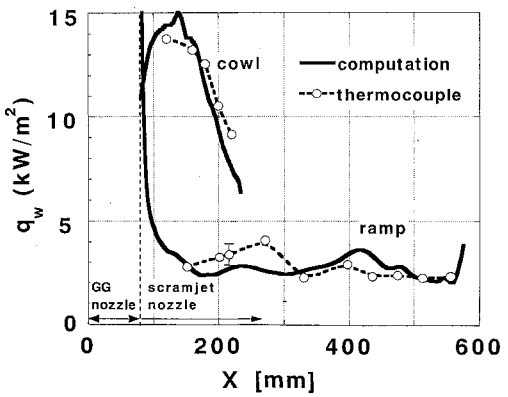

Fig. 7 Comparison of local heating rates on the scramjet nozzle. The computational results are shown by solid lines.

The skin friction coefficients on the nozzle walls can be calculated from the heat-flux. The experimental results obtained by the thermocouples showed the skin friction coefficient varying from 3 × 10^{-3} to 1 × 10^{-3} on the ramp. This result coincided with the numerical results and the experimental results found by the direct measurements of the boundary-layer thickness (Fig. 7 in Ref. 1). Spaid et al.[6] measured the skin friction by a rake probe and found higher values of 1.48 × 10^{-3} and 1.51 × 10^{-3} compared with their estimation (1.1 × 10^{-3}) using the van Driest method. In our study, the integral method proposed by Spalding and Chi gave a skin friction of 3 × 10^{-3} to 0.9 × 10^{-3} in the present experiment. The measurements of the velocity profiles on the ramp confirmed the present results.

Effects of Nozzle External Flows

Effects of external flow conditions on the pressure and the surface streamline (oil-flow) patterns are shown in Fig. 8. The left part (Fig. 8a) presents the isobaric contour lines and the right part (Fig. 8b) the oil-flow under the four external conditions, A–D defined in Table 2. Each consists of the side-fence and the ramp. The detailed pressure patterns for case A can be found in Fig. 6.

The optimum values of NPR in the nozzle examined are 300 at the ramp and 80 at the cowl end. Therefore, cases A and B are in underexpanded conditions. The lower ambient pressure affects the pressure distributions in the vicinity of trailing edge of the ramp. In cases B and D, the external flow of Mach 6 is deflected on the external wall of the ramp and produces a shock wave. The shock wave increases the environmental pressure at the trailing edge of the ramp. The reason why the depression region found at the ramp trailing edge in case A shrinks in case B is that the increased back pressure reduces the region influenced upstream via the boundary layer.

In the overexpanded flow condition of case D, the high environmental pressure causes the flow separation at the ramp trailing edge. The oil-flow of case D indicates that the separated flow reattaches and forms a two-dimensional separation bubble. The static pressure at the cowl trailing edge is higher than the environmental pressure in case D. The flowfields on the cowl and the side-fences do not change from those in cases A and B because of the external flow with a high Mach number of 6.

Another case of the overexpanded nozzle flow, case C, shows the fairly peculiar pressure and oil-flow patterns. A V-shaped pressure distribution and crossflows appear on the ramp wall. The oil-flow on the sidewall indicates that a cross-flow is initiated at the corner between the sidewall and the cowl plate. The entrainment of the still air from the environment generates a separation vortex and the inward flow induces an oblique shock on the side fence. The external flow with a lower Mach number enhances the separation vortex because the lower Mach number flow has to deflect with a larger angle for equilibration with the high ambient pressure. This is the reason why the separated flow does not appear on the side-fences and the effect of the external flow is confined to the narrow region in case D.

Discussion

Nozzle Flow in the Overexpanded, Low Mach Number Flow

For case C, two separation shocks are formed on the sidewalls by the entrained external flow. The sidewall separation

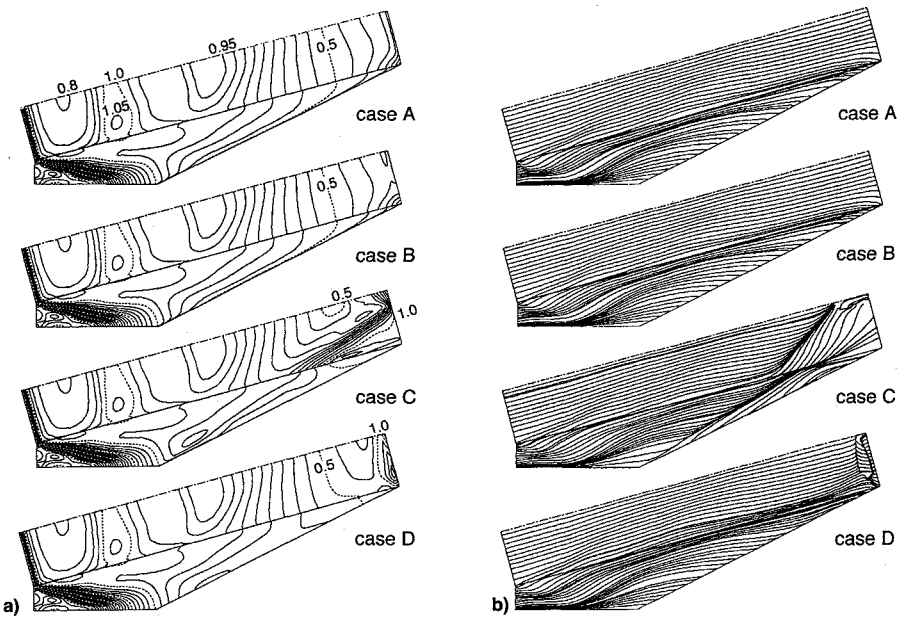

Fig. 8 Effects on a) wall pressure distributions and b) the surface streamlines of external flows given in Table 2.

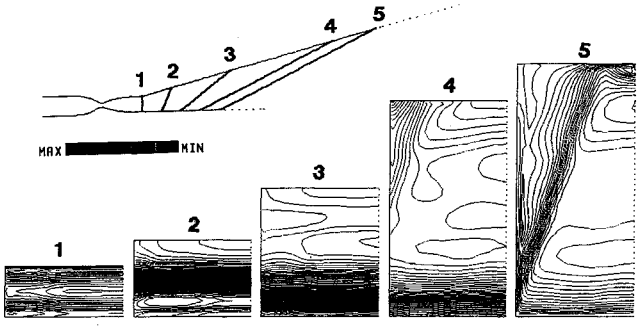

Fig. 9 Isobaric contours at different cross sections in case C. Stations 1 and 4 correspond to the entrance and the exit of the scramjet nozzle, respectively.

line can be observed in the oil-flow given by Fig. 8b. The surface streamlines initially converge toward the separation line and then diverge from it, which indicates the entrainment flow from the ambient air. The shock waves associated with the separation vortices are located upstream of the separation line. The pressure rise due to the shock induces the secondary flow to the ramp on the sidefences. The ramp separation line and the oblique shock can be seen in Fig. 8b.

Isobaric contours calculated on five cross sections (y-z planes) are illustrated in Fig. 9 for case C. Station 1 coincides to the inlet of the scramjet nozzle, and station 4 corresponds to the exit of the scramjet nozzle. The right sides in the cross sections are the symmetric plane of the nozzle. The separation shock wave, propagating from the left-upper corner to the symmetric plane, can be found at stations 4 and 5. The pair of shock waves forms a crossing shock wave above the ramp wall. The reflection of the crossing shock wave on the ramp generates the inverse V pattern in the isobaric contour at station 5.

The interaction between the secondary flow from the sidefences to the ramp with the nozzle core flow evolves another separation line and the three-dimensional high-pressure region on the ramp. The streamlines converging to the centerline of the ramp are associated with the high-pressure region. A blowing up of the surface flow at the symmetric plane (separation bubble) and a reverse flow in the separation bubble at the ramp trailing edge were observed in the velocity-vector map calculated for case C.

Another shock wave might be formed above the bubble if the pressure increase is large enough. The expansion fan initiated by the ramp deflection reflects back as a compression wave from the free-shear layer developed from the cowl trailing edge. Decreasing NPR, the compression or shock wave might impinge on the ramp. Thus, three or four shock waves are formed which confine the nozzle flow in an overexpanded, rectangular nozzle. The flow with the Mach reflection and the side-fence separation can be found in the oil-flows by Carson and Mason.[3]

The pressure distribution seen in case C of Fig. 8 was observed in the experiment by Hiraiwa et al.[2] They found that the thrust did not deteriorate so rapidly with decreasing NPR. The wall pressure measured on the ramp showed a high-pressure region caused by the separation flow from the sidewalls, when the nozzle pressure was decreased slightly from the ambient pressure. The three-dimensional high-pressure region in the ramp yielded a nozzle performance 10% superior to that assuming two-dimensional separation.

This improved nozzle performance and the change of the pitching moment are strongly dependent on the Mach number of the external flow. The entrainment on the sidewalls becomes evident in the flight with a low Mach number. Hypersonic vehicles are required to fly at low altitude with a low Mach number. Therefore, the variations of nozzle performance and the pitching moment delivered under off-design conditions must be accounted for in scramjet nozzles.

Comparison of Nozzle Performances

Table 1 summarizes the nozzle performance expressed by the specific impulse in the unit of velocity. The thrust delivered by the inviscid core flow is also tabulated for comparison with the experimental results. The ODE code provides the theoretical value of 57.27 m/s for the nozzle examined (T_0 = 293 K). The experimental I_{sp} delivered by the core flow was found to be 54.0 m/s, which showed the divergence loss to be 3.27 m/s (5.7%). The inviscid I_{sp} derived by TVD3D was 53.0 m/s. The discrepancy of the TVD3D value from the experimental results was found to be 2.0%. It can be concluded that the performance by the core flow was successfully reproduced by the TVD3D code.

The boundary-layer integral method was adopted in JANNAF to evaluate the friction loss on the ramp wall. The loss was 2.0 m/s, which was in good agreement with the estimation from the velocity profile measurements. The TVD3D calculation yielded a value of 1.62 m/s. The friction which worked on the cowl was found to be greater than that on the ramp in spite of the smaller wetted area. The friction on sidewalls

was overestimated to be 6.6 m/s in the JANNAF. A smaller value of 3.50 m/s was obtained by the TVD3D code.

The total friction loss can be accessed by subtracting the thrust measured by load-cells from the pressure-integral thrust experimentally. The total friction loss was predicted to be 7.56 m/s by TVD3D, which is comparable with the experimental value (6.6 m/s). The 88% overestimation of the friction loss with the JANNAF code was reduced to 13% in the TVD3D evaluation. Finally, delivered I_{sp} was 45.4 m/s (TVD3D). The I_{sp} calculated by TVD3D coincided with the experimental value with a discrepancy of 4.2%. Therefore, the nozzle performance of the nozzle internal flow could be predicted accurately.

In order to discuss the nozzle performance under off-design conditions, the thrust should be corrected considering the back pressure on the nozzles. The correction is given by $\int P_a \, dA = (\Delta c^*)/\mathrm{NPR}$, where the increment of expansion ratio in scramjet nozzles and the characteristic velocity are denoted by Δ and c^*, respectively. Table 2 shows the core flow I_{sp} (pressure thrust) and the delivered I_{sp}, as well as the correction and the friction loss calculated by the TVD3D code for the various external flow conditions. The decrease in NPR from 968 to 96.8 produces a "bubble"-type separation in the nozzle and reduces the friction loss in the nozzle. In case C, showing the separated flow on the sidewalls, the friction loss on the sidewalls decreases by 6% compared with case A.

Table 2 indicates that the I_{sp} delivered by the scramjet nozzle is positive in cases A and B, but becomes negative in cases C and D with NPR = 96.8. This implies that the overexpansion loss causes the nozzle performance to deteriorate and fall below that of the gas generator with a smaller nozzle area ratio. Regarding the evaluation of the overexpansion loss in case C, since the I_{sp} delivered by the scramjet nozzle is given as -18.9 m/s, the reduction of 64.2 m/s from the core flow I_{sp} (45.4 m/s) is the overexpansion loss. This evaluated value for the overexpansion loss agrees well with the experimental value (64.0 m/s). The smaller loss compared with case D (-23.4 m/s) results from the high-pressure region by the crossing shock wave.

Conclusions

Three-dimensional codes incorporated by the Baldwin-Lomax model were utilized for simulating the flowfield in the scramjet nozzles. Comparisons with the experimental results led to the following conclusions.

1) Pitot and static pressure distributions at the inlet of scramjet nozzles were calculated for comparison with the experimental results. Although the numerical code provided satisfactory results, the numerical results yielded distributions which were flatter than the experimental ones. Wave patterns calculated shifted upstream.

2) The heat fluxes evaluated by the viscous code were found to agree with the experimental results measured by thermocouples. The skin friction also coincided with those estimated from the heating rates as well as with the estimation by the Spalding integral method.

3) Under overexpanded conditions for scramjet nozzles, a pair of separation shocks is produced on the sidewalls. The shock waves, blocking the nozzle exit plane, deflect the nozzle flow upward and inward. The crossing shock waves from the sidewalls produce a high pressure on the nozzle ramp. The high-pressure region results in superior nozzle performance and yields unexpected pitching moment under overexpanded flight condition.

4) The numerical results showed the friction loss to be 13.2% in the scramjet nozzle examined. The experimental results and the numerical calculations were in close agreement within a discrepancy of 4.2% for the nozzle internal flow performance. The evaluated overexpansion loss agreed well with the experimental data under the condition examined.

Acknowledgments

This study was conducted as a joint research with Ishikawajima-Harima Heavy Industries, Co., Ltd. The authors thank Sadatake Tomioka at the Kakuda Research Center for his useful comments.

References

[1]Mitani, T., Ueda, S., Tani, K., Sato, S., Miyajima, H., Matsumoto, M., and Yasu, S., "Validation Studies of Scramjet Nozzle Performance," *Journal of Propulsion and Power*, Vol. 9, No. 5, 1993, pp. 725–730.

[2]Hiraiwa, T., Ueda, S., Sato, S., Mitani, T., Yamamoto, M., and Matsumoto, M., "Off-Design Performance of Scramjet Nozzles," International Symposium on Air Breathing Engine, ISABE Paper 93-7108, Sept. 1993.

[3]Carson, G. T., Jr., and Mason, M. L., "Experimental and Analytical Investigation of a Nonaxisymmetric Wedge Nozzle at Static Conditions," NASA TP 1188, July 1978.

[4]Carson, J. R., and Abdol-Hamid, K. S., "Prediction of Internal Performance for Two-Dimensional Convergence-Divergence Nozzles," AIAA Paper 91-2369, June 1991.

[5]Lai, H., "3D Computation of Hypersonic Nozzle," AIAA Paper 90-5203, Oct. 1990.

[6]Spaid, F. W., and Keener, E. R., "Experimental Results for a Hypersonic Nozzle/Afterbody Flowfield," AIAA Paper 92-3915, July 1992.

[7]Spaid, F. W., and Keener, E. R., "Hypersonic Nozzle/Afterbody CFD Code Validation, Part 1: Experimental Measurements," AIAA Paper 93-0607, Jan. 1993.

[8]Baysal, O., and Engelund, W. C., "Viscous Computations of Cold Air/Air Flow Around Scramjet Nozzle Afterbody," NASA CR 4406, Oct. 1991.

[9]Huebner, L. D., and Tatum, K. E., "Computational Experimental Aftbody Flow Fields for Hypersonic, Airbreathing Configurations with Scramjet Exhaust Flow Simulation," AIAA Paper 91-1709, June 1991.

[10]Watanabe, S., "Scramjet Nozzle Experiment with Hypersonic External Flow," *Journal of Propulsion and Power*, Vol. 9, No. 4, 1993, pp. 521–528.

[11]Ruffin, S., and Spaid, F. W., "Hypersonic Single Expansion Ramp Nozzle Simulations," *Journal of Spacecraft and Rockets*, Vol. 29, No. 6, 1992, pp. 749–755.

[12]Mikkelsen, K. L., and Idzorek, J. J., "Experience in the Operation of a Hypersonic Nozzle Static Thrust Stand," AIAA Paper 92-3292, 1992.

[13]Monta, W. J., "Pitot Survey of Exhaust Flow Field of a 2D Scramjet Nozzle at Mach 6 with Air or Freon and Argon Used for Exhaust Simulation," NASA TM 4361, Aug. 1992.

[14]*JANNAF Rocket Engine Performance Prediction and Evaluation Manual*, Chemical Propulsion Information Agency, The Johns Hopkins Univ., CPIA 246, Silver Spring, MD, April 1975.

[15]Marvin, J. G., "Turbulence Modeling for Hypersonic Flow," *Advances in Hypersonics*, edited by J. J. Bertin, J. Periaux, and J. Ballmann, Vol. 2, Birkhauser, Boston, MA, 1992.

[16]Garrison, T. J., Settles, G. S., Narayanswami, N., and Knight, D. D., "Structure of Crossing-Shock-Wave/Turbulent-Boundary-Layer Interactions," *AIAA Journal*, Vol. 31, No. 12, 1993, pp. 2204–2211.

[17]Kussoy, M. I., Horstman, K. C., and Horstman, C. C., "Hypersonic Crossing-Shock Wave/Turbulent-Boundary Layer Interactions," *AIAA Journal*, Vol. 31, No. 12, 1993, pp. 2197–2203.

[18]Narayanswami, N., Hortman, C. C., and Knight, D. D., "Numerical Simulation of Crossing-Shock Wave/Turbulent Boundary Layer Interaction at Mach 8.3—Comparison of Zero- and Two-Equation Turbulent Models," AIAA Paper 93-779, Jan. 1993.